Electronic Supplementary Information (ESI)

Bimetallic Co-Mo sulfide/carbon composites derived from polyoxometalate encapsulated polydopamine-decorated ZIF nanocubes for efficient hydrogen and oxygen evolution

Zheng Huang,[a] Zhuxian Yang,[a] Quanli Jia,[b] Nannan Wang,[c] Yanqiu Zhu[a] and Yongde Xia*[a]

[a] *College of Engineering, Mathematics and Physical Sciences, University of Exeter, Exeter EX4 4QF, United Kingdom. Email: y.xia@exeter.ac.uk*

[b] *Henan Key Laboratory of High Temperature Functional Ceramics, Zhengzhou University, Zhengzhou, 450052, PR China*

[c] *GIFT (Guangxi Institute for Fullerene Technology), Key Laboratory of New Processing Technology for Nonferrous Metals and Materials, Ministry of Education, School of Resources, Environment and Materials, Guangxi University, Guangxi, 530004, China*

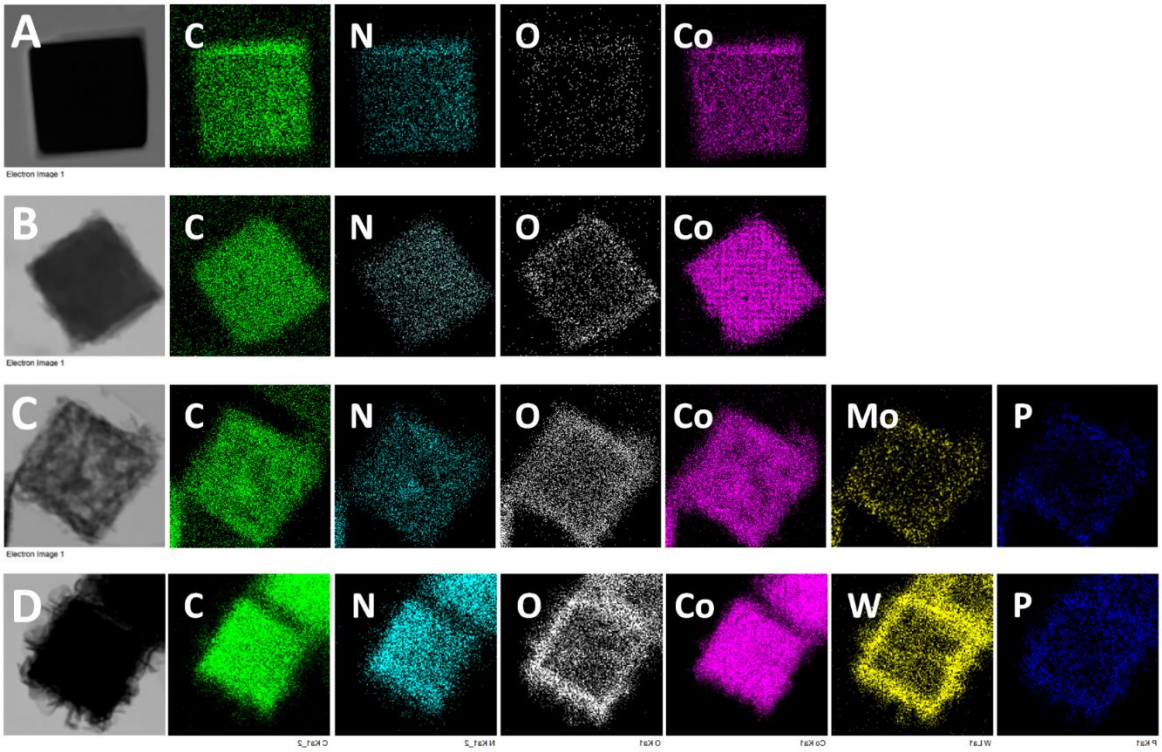

Fig. S1 Elemental mappings of A) Z67, B) Z67-D, C) Mo-Z67-D and D) W-Z67-D.

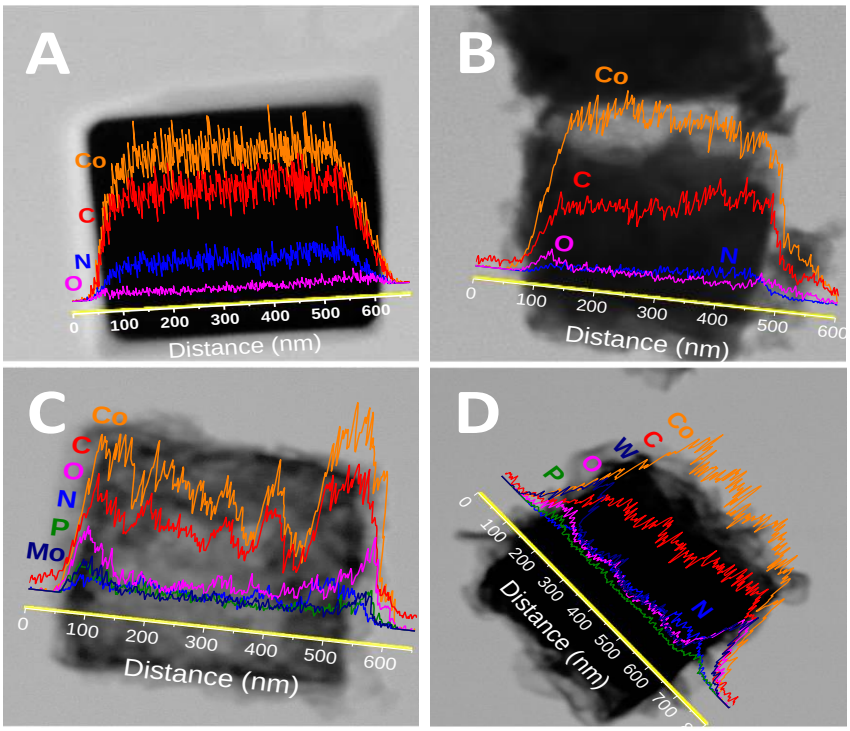

Fig. S2 TEM images and elemental line profiles of A) Z67, B) Z67-D, C) Mo-Z67-D and D) W- Z67-D.

Elemental line scanning for individual cubic particles was conducted during TEM-EDX analysis and the results are in line with the TEM images and elemental mappings. For Z67 (Fig. S2A), all the elements distribute evenly across the cubes. With PDA coating, small amount of O and C is found at the edge of the Z67-D cubes (Fig. S2B). The slightly uneven distribution of Co and C reveals that PDA coating could lead to mild dissociation of ZIF-67, which has been reported previously [1, 2]. The overlapped edge region of Co and O spectrum indicates the chelation of Co on coated PDA. On the other hand, the uneven distribution of Co, C, N across the Mo-Z67-D in the line spectra (Fig. S2C) suggests that the PMA penetrates through the PDA coating and generates cavities in the core by acid etching. Weak peaks of O, P and Mo on the edge of cubes imply that some PMA molecules have chelated with coated PDA. Whereas for W-Z67-D (Fig. S2D), elements O, P, W are mainly distributed at the edge of the cubes and Co, C, N are mainly distributed in the middle of the cubes with mild variation, which suggests that the majority of PTA molecules are chelated with the coated PDA.

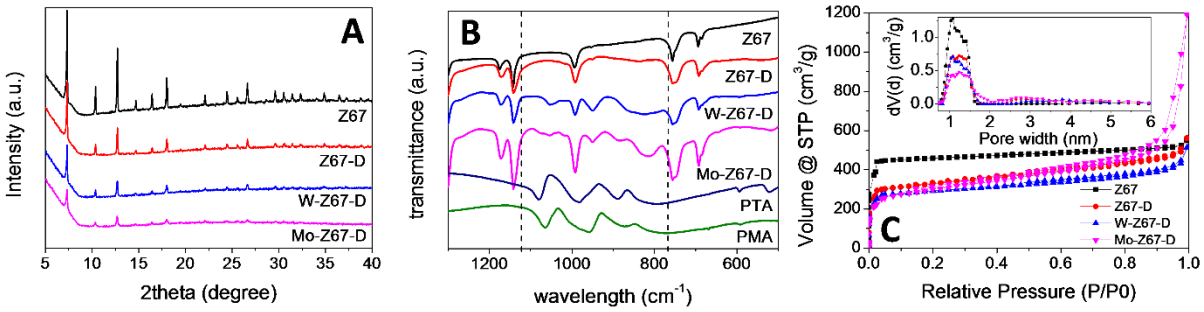

Fig. S3 A) XRD patterns of the as-made Z67, Z67-D, W-Z67-D and Mo-Z67-D; B) FT-IR spectra of PTA, PMA and four as-made samples; C) Nitrogen sorption isotherms and the DFT pore size distribution (insert) of the as-synthesized Z67, W-Z67-D and Mo-Z67-D.

Table S1 BET surface area and total pore volume of the four as-made samples.

Sample	**Z67**	**Z67-D**	**W-Z67-D**	**Mo-Z67-D**
BET Surface Area, S_{BET} (m^2 g^{-1})	1549	1123	993	1037
Total pore volume, V_{total} (cm^3 g^{-1})	0.85	0.87	0.80	1.84

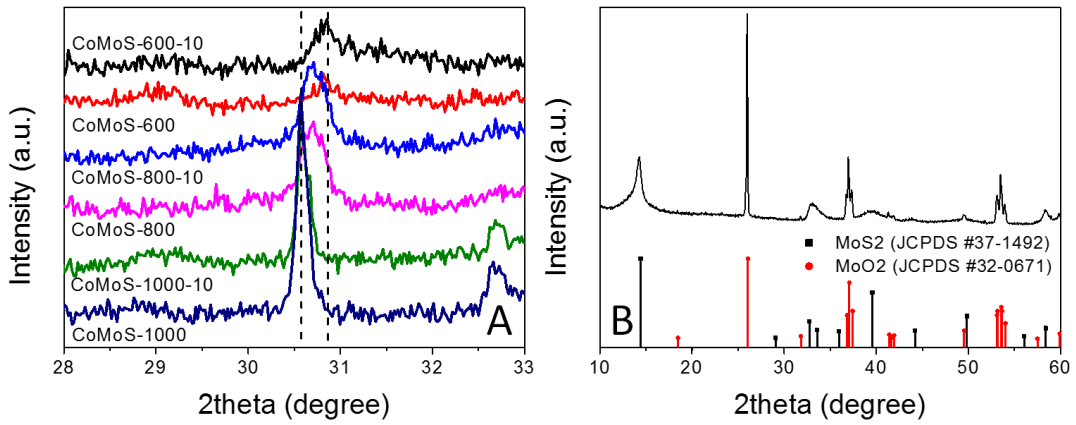

Fig. S4 A) XRD peak shifts and asymmetrical peak broadening observed in Mo-Z67-D derived samples as the heat treatment temperature and heating ramp rate changed; B) XRD pattern of PMA-C (PMA calcined at 800 °C in H_2S/Ar atmosphere).

As shown in Fig. S4B, PMA-C obtained from heat treatment of pure PMA powder in H_2S/Ar atmosphere at 800 ^oC demonstrates XRD characteristic peaks of MoS_2 (JCPDS #37-1492) and MoO_2 (JCPDS #32-0671).

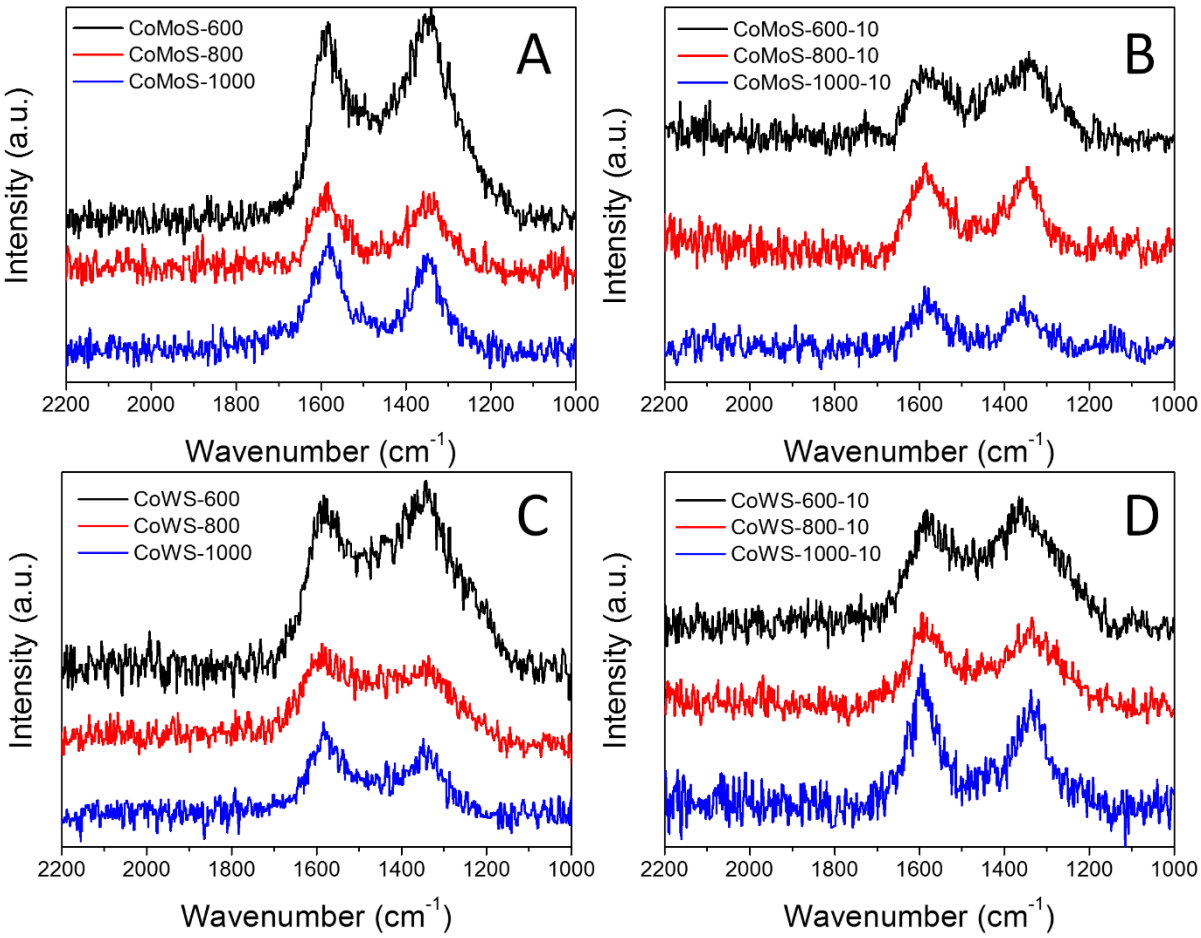

Fig. S5 Raman spectra of A) CoMoS-600, CoMoS-800, CoMoS-1000; B) CoMoS-600-10, CoMoS-800-10, CoMoS-1000-10; C) CoWS-600, CoWS-800, CoWS-1000 and D) CoWS-600-10, CoWS-800-10, CoWS-1000-10.

Table S2 I_D/I_G ratio of Mo-Z67-D and W-Z67-D nanocubes derived samples.

Precursor		Mo-Z67-D		W-Z67-D	
Pyrolysis temperature	**Heat ramp rate**	**10 °C/min**	**2 °C/min**	**10 °C/min**	**2 °C/min**
600 °C		1.17	1.06	1.11	1.08
800 °C		0.96	0.91	0.95	0.87
1000 °C		0.86	0.84	0.84	0.83

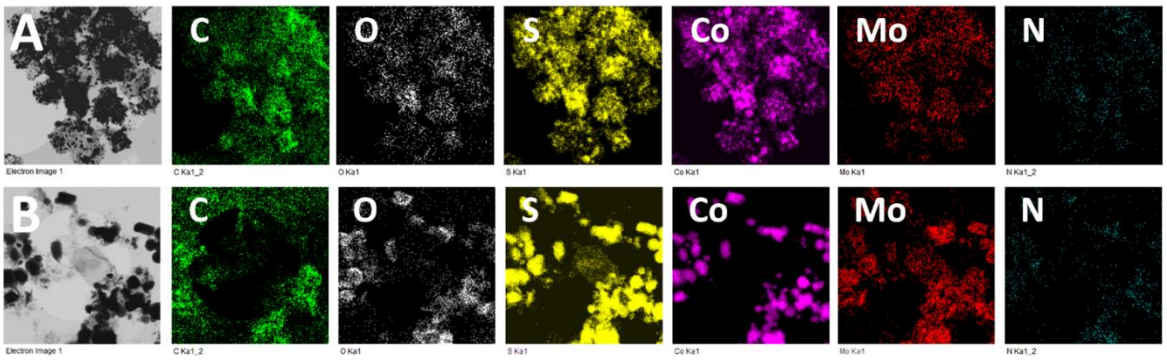

Fig. S6 TEM elemental mappings of A) CoMoS-800 and B) CoMoS-1000.

Table S3 TEM-EDX results and Co/Mo ratio of Mo-Z67-D and CoMoS-600.

Mo-Z67-D		CoMoS-600	
Element	**Atomic%**	**Element**	**Atomic%**
C	50.35	C	45.21
Co	11.54	Co	14.62
Mo	2.51	Mo	3.28
Co/Mo	4.60	**Co/Mo**	4.46

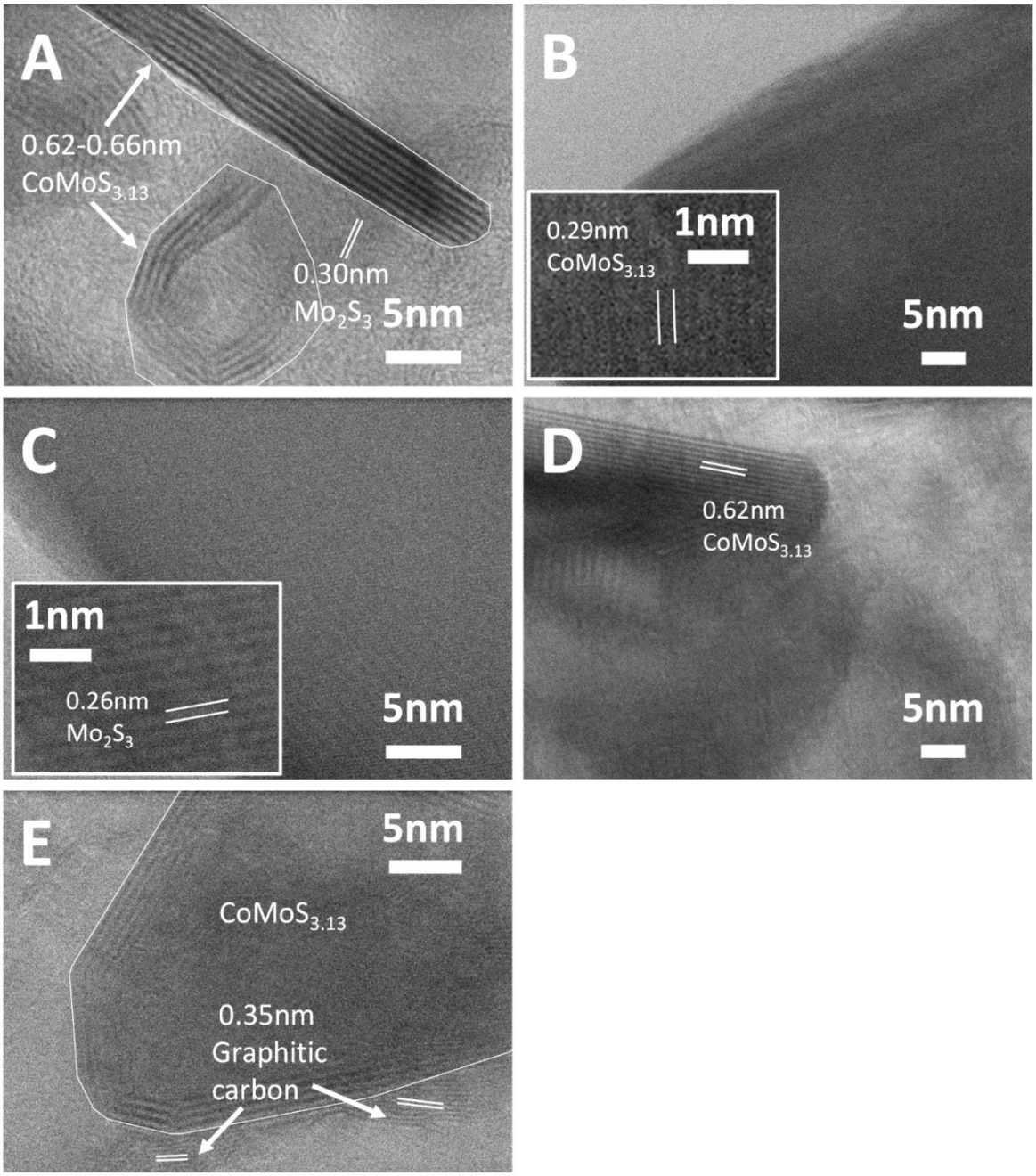

Fig. S7 High resolution TEM images of A) $CoMoS_{3.13}$ and Mo_2S_3 crystals in CoMoS-800; agglomerated B) $CoMoS_{3.13}$ crystal and C) Mo_2S_3 crystals in CoMoS-1000; D) fine $CoMoS_{3.13}$ crystal on the carbon matrix of CoMoS-1000 and E) graphitic carbon in CoMoS-1000.

Table S4 Textural properties of Co-Mo-S/C samples obtained from N_2 sorption analysis.

Sample	CoMoS-600	CoMoS-800	CoMoS-1000
BET surface area ($m^2\ g^{-1}$)	76	147	128
Total pore volume ($cm^3\ g^{-1}$)	0.21	0.48	0.26

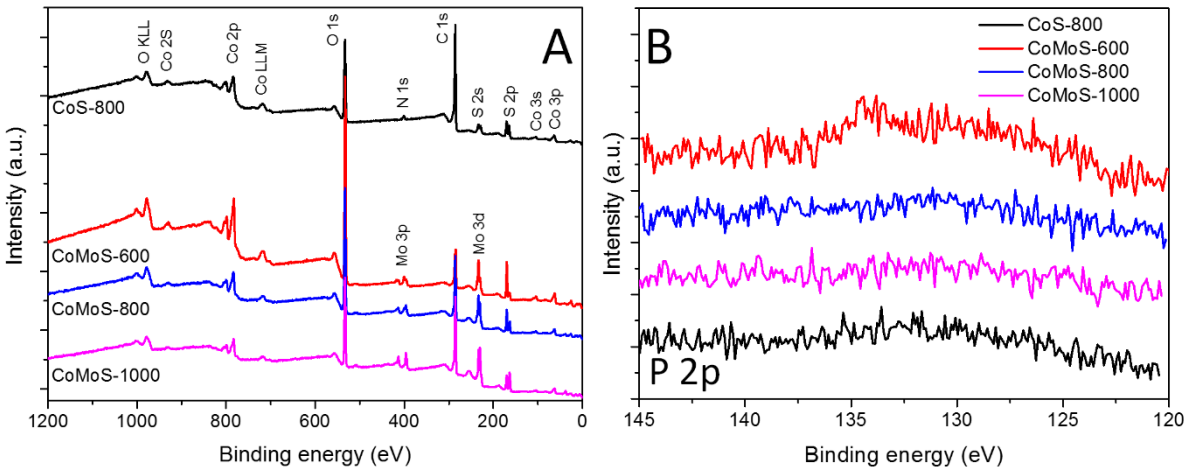

Fig. S8 A) XPS element survey and B) high-resolution P 2p spectra of samples CoS-800, CoMoS-600, CoMoS-800 and CoMoS-1000.

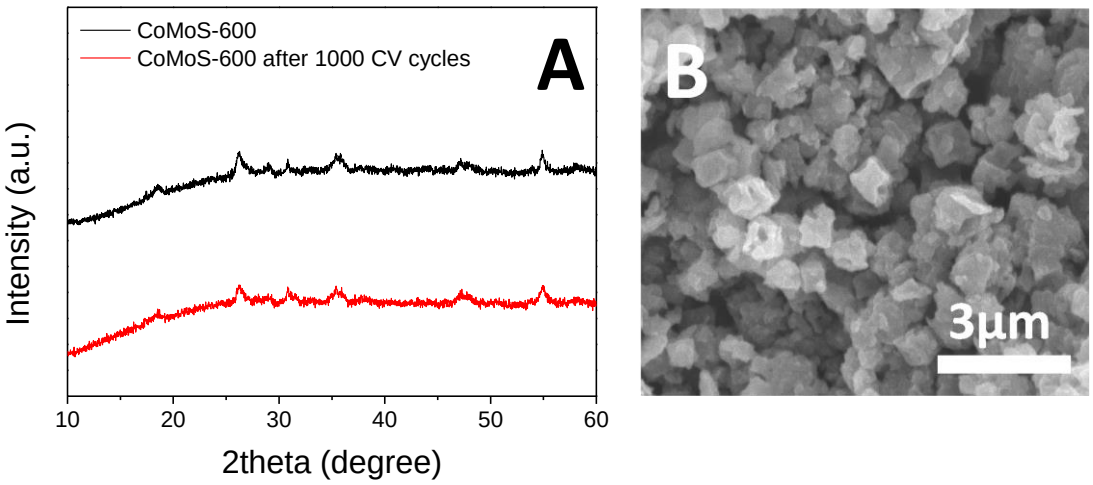

Fig. S9 A) XRD pattern of MoCoS-600 before and after 1000 CV cycles, B) SEM image of MoCoS-600 after 1000 CV cycles.

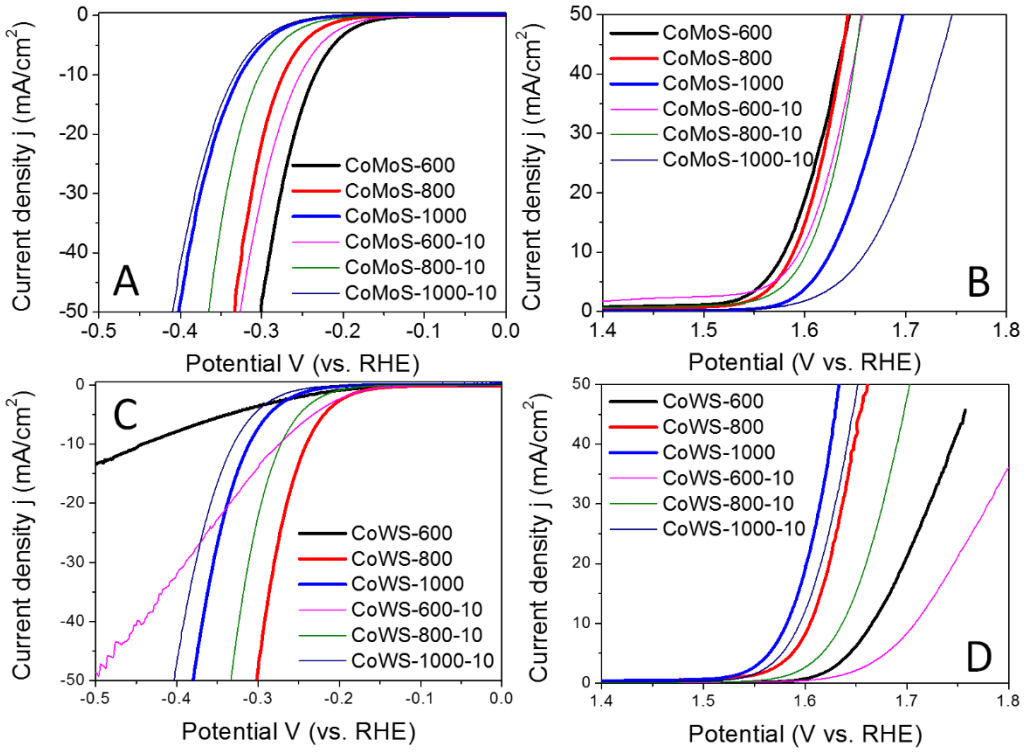

Fig. S10 A) HER and B) OER polarization curves of Mo-Z67-D derived Co-Mo-S/C composites obtained at different pyrolysis temperatures and two different heating ramp rates; C) HER and D) OER polarization curves of W-Z67-D derived Co-W-S/C composites obtained at different pyrolysis temperatures and two different heating ramp rates.

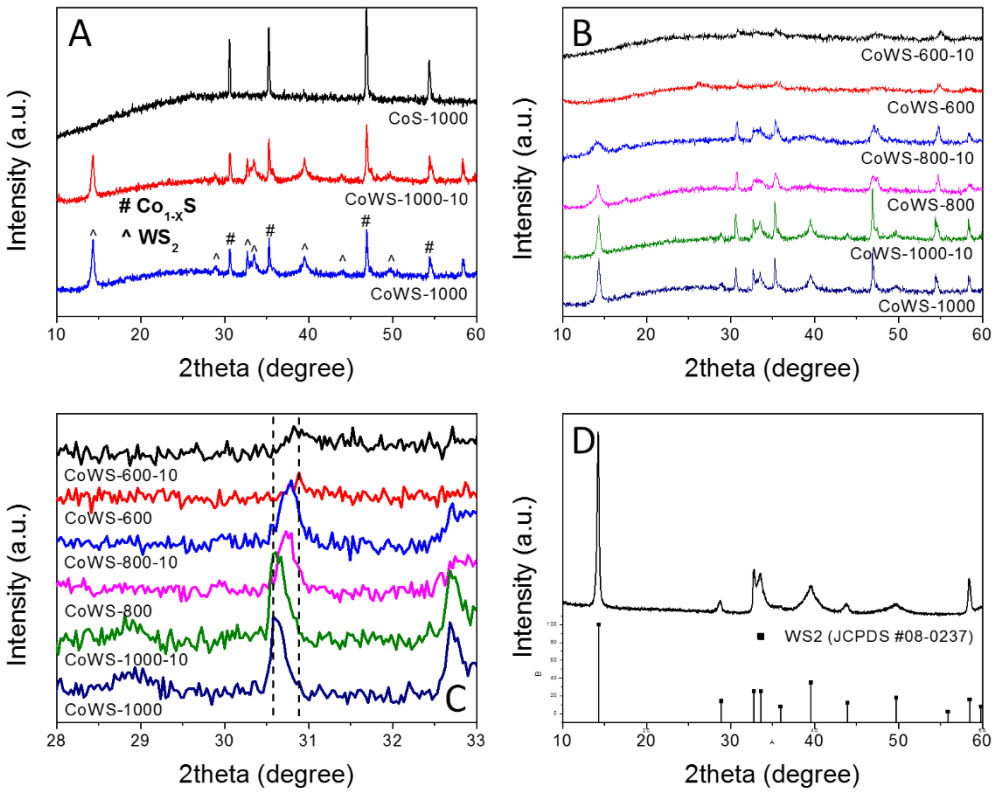

Fig. S11 XRD patterns of A) CoS-1000, CoWS-1000-10 and CoWS-1000, B) W-Z67-D derived Co-W-S/C samples obtained at different pyrolysis temperatures and ramp rates, C) enlarged XRD peak shifts of W-Z67-D derived Co-W-S/C samples at different heat treatment temperatures and ramp rate and D) PTA-C.

The as-synthesized W-Z67-D was subjected to similar heat treatments applied to Mo-Z67-D. XRD patterns in Fig. S11A show that the derived samples are mainly composed of $Co_{1-x}S$ (JCPDS #42-0826) and WS_2 (JCPDS #08-0237), whereas only $Co_{1-x}S$ (JCPDS #42-0826) is observed in the Z67-D derived composite. Similar to Mo-Z67-D derived composites, high heat treatment temperatures and slow heating ramp rates result in metal sulfides with better crystallinity and larger grain size, which is supported by the narrower and sharper characteristic

diffraction peaks of the obtained composites (Fig. S11B). The detailed XRD patterns (Fig. S11C) suggest that the change of the asymmetrical main peaks and the shift in peak position are clearly observed, which may be due to the lattice distortions and crystallographic defects of the crystalline components.

It is worth noting that the direct heat process of pure PMA and PTA powder in H_2S/Ar leads to distinct different samples: PMA-C (Fig. S4B) exhibits mixed composition phases including metal dichalcogenides and metal oxide, whereas PTA-C (Fig. S11D) only consists of pure metal dichalcogenides phase. This difference is also reflected in the compositions of the PMA/PTA modified Z67-D derivatives.

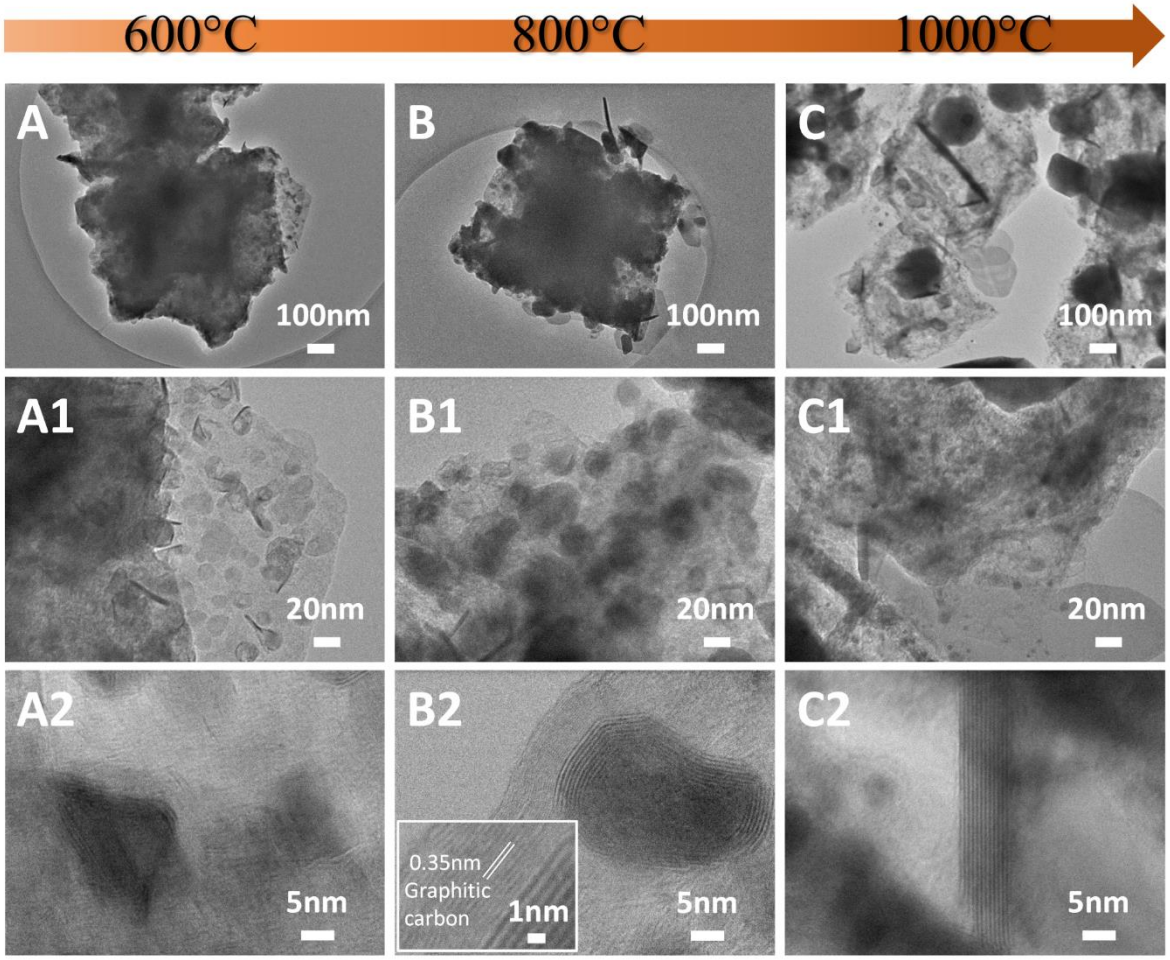

Fig. S12 TEM images of A) & A1): CoWS-600, B) & B1): CoWS-800 and C) & C2): CoWS-1000; high resolution TEM image of A2): CoWS-600, B2): CoWS-800 and C2): CoWS-1000.

TEM images of Co-W-S/C composites are presented in Fig. S12. At 600 °C (Fig. S12A and A1), small nanocrystals of size around 20 nm are formed on the carbon matrix, without observable agglomerated large crystals at the edge of the carbon support. At 800 °C (Fig. S12B), agglomeration of $Co_{1-x}S$ crystals and WS_2 flakes are observed. The size of the small nanocrystals in the carbon matrix turns larger and thicker, with maximum diameters around 50 nm (Fig. S12B1). When the pyrolysis temperature increases to 1000 °C (Fig. S12C), most metal

compounds are separated from the carbon matrix and agglomerated into large $Co_{1-x}S$ spheres with average diameters of 200 nm, accompanied with WS_2 flakes with diameter up to 400 nm and thickness up to 40 nm. Moreover, a large amount of ultra-small crystals with sizes under 5 nm remain in the carbon matrix (Fig. S12C1), which allow more exposed active sites during the electrochemical process, contributing to the enhanced OER performance of the CoWS-1000.

The crystallinity of the WS_2 improves at elevated pyrolysis temperature, leading to the transformation of the lattice spacing as shown in Fig. S12A2, B2 and C2. Obviously, fewer defects exist in the crystal of the composites obtained at higher pyrolysis temperature, which can cause deterioration in electrochemistry performance, as suggested by Ling et al. [3]. However, unlike the defect-rich sample CoMoS-600, which outperforms the CoMoS-800 in HER performance, sample CoWS-800 displays better HER activity than the defect-rich CoWS-600. It may be due to the fact that graphitic carbon was formed in CoWS-800 (Fig. S12B2 insert), whereas no graphitic carbon was observed in CoMoS-800 (Fig. S7A). This difference in the degree of graphitization is also verified by the corresponding I_D/I_G value, as shown in Table S2.

TEM elemental mappings of Co-W-S/C samples are shown in Fig. S13**.** Elements C, O, S, Co, W and N are found in all three composites, and all elements distribute evenly throughout the composites.

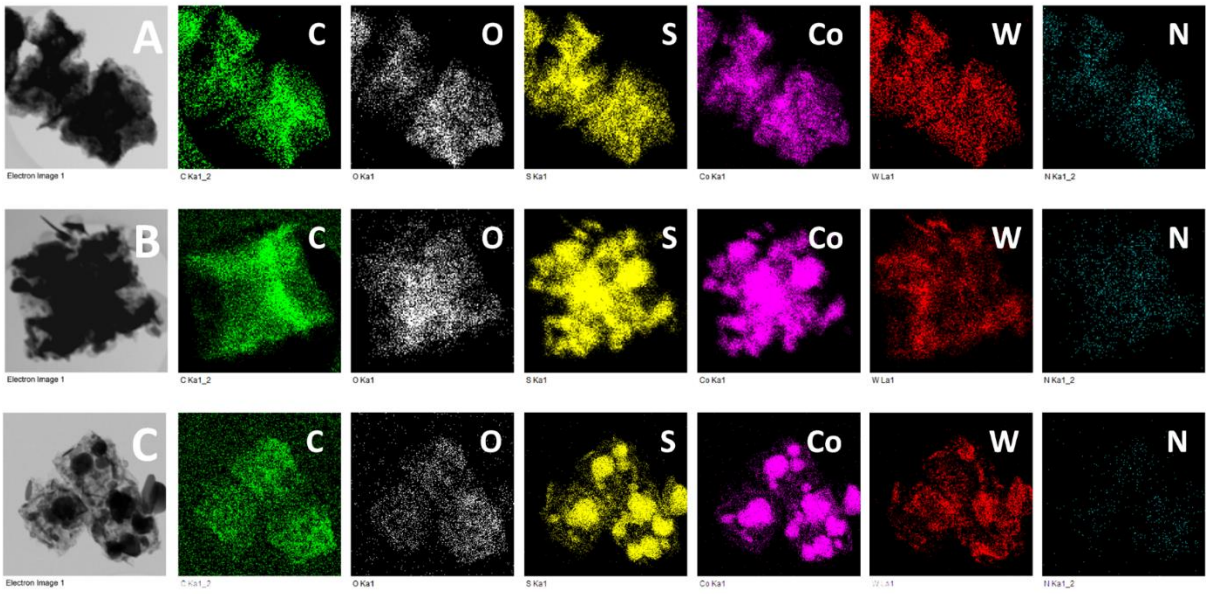

Fig. S13 TEM elemental mappings of A) CoWS-600, B) CoWS-800 and C) CoWS-1000.

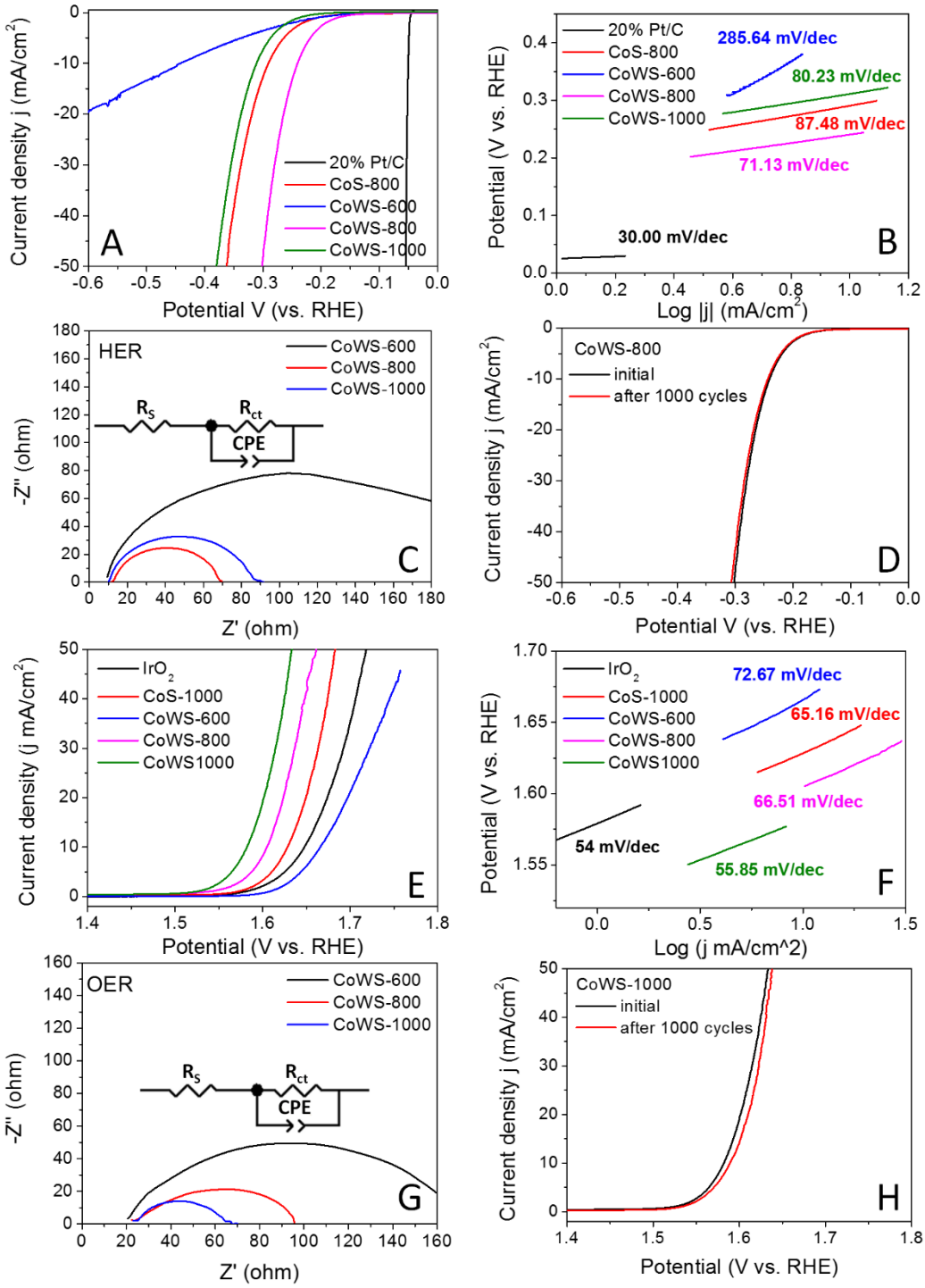

Fig. S14 A) HER polarization curves and B) corresponding Tafel plots of the benchmark 20% Pt/C, CoS-800, CoWS-600, CoWS-800 and CoWS-1000; C) EIS of CoWS-600, CoWS-800 and CoWS-1000; D) Polarization curves of CoWS-800 before and after 1000 CV cycles. All polarization curves are iR corrected and obtained in 0.5 M H_2SO_4 electrolyte; E) OER

polarization curves and F) corresponding Tafel plots of the benchmark IrO_2, CoS-600, CoWS-600, CoWS-800 and CoWS-1000; G) EIS of CoWS-600, CoWS-800 and CoWS-1000; H) Polarization curves of CoWS-600 before and after 1000 CV cycles. All polarization curves are iR corrected and obtained in O_2-saturated 1 M KOH electrolyte.

In the HER LSV curves in Fig. S14A and Tafel slopes in Fig. S14B, composite CoWS-800 shows the smallest onset potential of -0.171 V, an overpotential of -0.240 V to achieve the current density of 10 mA cm^{-2} and Tafel slope of 71.13 mV dec^{-1}, which is much smaller than those of W-free CoS composites obtained under the same heat treatment conditions. EIS of three Co-W-S/C samples shows R_{ct} of 171.5 Ω, 54.89 Ω and 72.35 Ω, respectively for samples CoWS-600, CoWS-800 and CoWS-1000 (Fig. S14 C), revealing that sample CoWS-800 possesses the fastest electron transfer rate at the electrode material and electrolyte interface. It is believed that the improved HER performance of CoWS-800 is due to the synergistic effect of highly graphitized carbon matrix (see Raman spectra in Fig. S5 and I_D/I_G ratio in Table S2) and large numbers of small WS_2 and $Co_{1-x}S$ nanoparticles that are encapsulated in or supported on the conductive carbon matrix (see TEM images in Fig. S12B).

On the other hand, composite CoWS-1000 shows the best OER activity amongst the Co-W-S/C composites, as indicated by the smallest onset potential of 0.293 V, an overpotential of 0.352 V to realize a current density of 10 mA cm^{-2} and Tafel slope of 55.85 mV dec^{-1}, as shown in Fig. S14E and F. Moreover, sample CoWS-1000 exhibits the smallest semicircle in the Nyquist plot (Fig. S14G), indicating the fastest electron transferability of this sample. It is likely that the ultra-small nanoparticles (< 5 nm, as shown in Fig. S12C1 and C2) embedded in the carbon matrix after 1000 °C heat treatment is the key toward the excellent OER

performance of this composite. In contrast, no such kind of ultra-fine nanoparticles is observed in sample CoMoS-1000.

The electrochemical HER and OER performance of Co-W-S/C composites are summarized in Table S5.

Table S5 HER and OER electrochemical performance of Co-W-S/C composites.

HER	**Onset potential @1 mA cm^{-2} (η_{onset}, V vs. RHE)**	**Overpotential @ 10 mA cm^{-2} (η_{10}, V vs. RHE)**	**Tafel slope (mV dec^{-1})**	**Charge transfer resistance (R_{ct}, Ω)**
20% Pt/C	-0.047	-0.050	30.00	-
CoS-800	-0.021	-0.291	87.48	-
CoWS-600	-0.021	-0.442	285.64	171.50
CoWS-800	-0.171	-0.240	71.13	55.85
CoWS-1000	-0.237	-0.311	80.23	72.35
OER	**Onset potential @1 mA cm^{-2} (η_{onset}, V vs. RHE)**	**Overpotential @ 10 mA cm^{-2} (η_{10}, V vs. RHE)**	**Tafel slope (mV dec^{-1})**	**Charge transfer resistance (R_{ct}, Ω)**
IrO_2	0.349	0.418	54.00	-
CoS-1000	0.340	0.398	65.16	-
CoWS-600	0.377	0.436	72.67	140.40
CoWS-800	0.307	0.375	66.51	71.48
CoWS-1000	0.293	0.352	55.85	37.40

References:

1. J. Ran, L. Xiao, W. Wu, Y. Liu, W. Qiu and J. Wu, *Nanotechnology*, 2016, **28**, 055604.
2. T. Wang, Y. He, Y. Liu, F. Guo, X. Li, H. Chen, H. Li and Z. Lin, *Nano Energy*, 2021, **79**, 105487.
3. Y. Ling, Z. Yang, Q. Zhang, Y. Zhang, W. Cai and H. Cheng, *Chem*, *Commun.*, 2018, **54**, 2631-2634.